Synthesis and Characterization of Multiferroic $BiFeO_3$-$CoFe_2O_4$ (BFO-CFO) composite thin film

A thesis submitted in partial fulfillment of the requirements for the award of the degree of

Masters of Technology

(Materials and Metallurgy Engineering)

Submitted by

Chetan Singh

Roll No. 601102003

Under the guidance of

Dr. Puneet Sharma

(Assistant Professor)

School of Physics and Materials Science

Thapar University, Patiala-147004,

Punjab.

How far you go in life depends on your being tender with the young, compassionate with the aged, sympathetic with the striving and tolerant of the weak and strong. Because someday in your life, you will have been all of these.

~~ ***George Washington Carver***

Dedicated to my parents and loving friends

DECLARATION

I hereby declare that the thesis entitled **"Synthesis and Characterization of Multiferroic $BiFeO_3$-$CoFe_2O_4$ (BFO-CFO) composite thin film"** is an authentic record of my own work for partial fulfillment of the award of the degree of M. Tech. (Materials Science and Metallurgical Engineering) under the supervision of ***Dr. Puneet Sharma,*** School of Physics and Materials Science, Thapar University, Patiala (Punjab), during January to June 2013.

The matter presented in this thesis has been not submitted in part or full to another University or Institute for the award of any degree.

Dated. 03/07/13

Chetan Singh

M. Tech (MME)

Roll. No. 601102003

Above statement and declaration made by candidate is correct to my knowledge and belief.

Dr. Puneet Sharma
Assistant Professor
School of Physics and Materials Science
Thapar University, Patiala (147004)

Countersigned by

Dr. Kulvir Singh
Hear and Associate Professor
School of Physics and Materials Science
Thapar University, Patiala (147004)

Dr. S. K. Mohapatra
Dean Academic Affairs
Thapar University, Patiala (147004)

ACKNOWLEDGEMENT

This master thesis was done in the School of Physics and Materials Science, Thapar University, and I wish to dedicate a few lines to thank every person who has helped and encouraged me during this period.

Firstly, I would like to express my great gratitude to my supervisor, Dr. Puneet Sharma for his endless and consistent guidance and encouragement. I really appreciate his efforts in imparting the knowledge of materials science and magnetic materials. The novel and creative ideas given by Dr. Puneet Sharma are indispensable to my research during the period of my candidature in the Department of School of Physics and Material Science.

I would like to thank Dr. Kulvir Singh, Professor and Head, School of Physics and Materials Science for his constant guidance and encouragement. I am also thankful to Dr. O. P. Pandey, Dr. B. N. Chudasama, Dr. S.D. Tiwari and all the faculty members of School of Physics and Materials Sciences for their constructive suggestions at different occassions.

Special thanks are due to Mr. Mintu Tyagi, PhD Scholar for showing me right path towards research and helping in lab work. My appreciation is also extended to my colleagues and friends. Their help and cooperation during my study will always be remembered.

More thanks will be given to my parents; I appreciate their spiritual support, which gives me a peaceful mind to finish my research.

C.S.

(Chetan Singh)

TABLE OF CONTENTS

LIST OF FIGURES

Chapter 4

ABSTRACT

In the present work, multiferroic (1-x) $BiFeO_3$–x ($CoFe_2O_4$) (x = 0, 0.1) Nano composite thin films were prepared by sol-gel spin coating process. Effect of volume ratio of CFO on the structural, electrical and magnetic properties of BFO/CFO composite thin film has been studied. X-ray diffraction study confirmed the co-existence of both perovskite $BiFeO_3$ (BFO) and spinel $CoFe_2O_4$ (CFO) phase. Atomic force microscopy shows a CFO particles distributed in BFO matrix. These composite thin films exhibit both ferroelectric and ferromagnetic properties at room temperature. The magnetic properties are improved by incorporation of CFO in BFO matrix. The saturation magnetization (M_s) increases with increasing x. For x = 0.1, M_s is found as high as ~ 40.12 emu/cm^3. Coercivity is increased with CFO concentration and found maximum (H_c ~ 127 Oe) for x = 0.10. Composite film shows ferroelectric behavior, however the ferroelectric properties are found to decrease with incorporation of magnetic phase.

CHAPTER 1

INTRODUCTION

As the name suggests multiferroic materials possess more than one of the so called ferroic properties. In recent year this term is commonly used for the material in which magnetism and ferroelectricity coexist. In 1894, P. Curie considered [1] that crystal could be simultaneously ferromagnetic and ferroelectric. The magnetization in the crystal can be induced by the application of electric field and vice versa. This effect is known as "magneto electric effect" [2] and the coupling between ferroelectric and magnetic interaction is known as "magneto electric coupling". It is clear from definition of magneto electric coupling that coexistence of ferroelectric and ferromagnetic order is a necessary condition for the material to be classified as magneto electric material. However, magneto electric coupling is an independent phenomenon that need not arise in all material that is both magnetically and electrically polarizable [3, 4].

$BiFeO_3$ (BFO) is a well-known multiferroic material that exhibits a distorted pervoskite structure with rhombohedral symmetry. Being a room temperature multiferroic (T_C = 1123 K and T_N = 643 K), it has been widely studied [5], [6], [7] and known to exhibit excellent ferroelectric properties with large remnant polarization as 100 μc/cm^2. Considerable drawback that limit their multifunctional applications is the weak magnetic behavior such as low saturated magnetization and remnant magnetization because of its G-type antiferromagnetic structure with nearest neighbor spins canting [8], [10]. So to improve the magnetic properties of BFO and $CoFe_2O_4$ (CFO) which is ferrimagnetic with cubic spinal structure is chosen to distribute among host BFO matrix, as CFO is reported to have large saturation magnetization [9] and have been used to improve the magnetic properties of the BFO thin films using several different approaches e.g. several layer-by-layer structures of BFO and $CoFe_2O_4$ [10, 40]. $CoFe_2O_4$ nanopillars embedded in $BiFeO_3$ [11]. Recently, an enhancement in magnetic behavior has been reported by distributing $CoFe_2O_4$ in BFO matrix synthesized by chemical solution deposition method [46]. Same approach has been used in this work to study the effect of volume ratio of CFO on magnetic properties; in addition emphasis given to its electrical behavior by sol gel method.

Thus, the objective of present study is to combining BFO and CFO phases, using sol-gel process. We have observed strong effect of the volume ratio of cobalt ferrite on the

magnetic behavior of such BFO/CFO composite thin films which exhibit excellent ferromagnetic

1.1 TYPES OF FERROICS

There are four types of ferroics:

- **FERROELECTRIC**

  These materials possess a spontaneous polarization that is stable and can be switched hysteretically by an applied electric field; antiferroelectric materials possess ordered dipole moments that cancel each other completely within each crystallographic unit cell.

- **FERROMAGNETIC**

  The materials which possess a spontaneous magnetization that is stable and can be switched hysteretically by an applied magnetic field; antiferromagnetic materials possess ordered magnetic moments that cancel each other completely within each magnetic unit cell is called ferromagnetic materials.

- **FERROELASTIC**

  These materials display a spontaneous deformation that is stable and can be switched hysterically by an applied stress.

- **FERROTOROIDIC**

  These materials possess a stable and spontaneous order parameter that is taken to be the curl of a magnetization or polarization. By analogy with the above examples, it is anticipated that this order parameter may be switchable. Ferrotoroidic materials have evaded unambiguous observation.

1.2 CLASS OF MULTIFERROICS

Generally multiferroics are categorized in two groups.

- **TYPE-I MULTIFERROICS**

  Type-I multiferroics are older and more numerous. These are often good ferroelectrics, and the critical temperatures of the magnetic and ferroelectric transitions can be well above room temperature. Unfortunately, the coupling between magnetism and ferroelectricity in these materials is usually rather weak. Some examples of Type-I multiferroic are $BiFeO_3$ (T_C~1103, T_N~643, P~90 μC/cm^2), $YMnO_3$ (T_c^{FE}~914 K, T_N~76, P~6μC/cm^2).

- **TYPE-II MULTIFERROICS ON BASIS OF ORIGIN OF FERROELECTRICITY IN THEM**

  The biggest excitement nowadays is caused by the discovery of a novel class of multiferroics in which ferroelectricity exists only in a magnetically ordered state and is caused by a particular type of magnetism [12, 13]. For example, in $TbMnO_3$ magnetic ordering appears at T_{N1} = 41 K, and at a lower temperature, T_{N2} = 28 K, the magnetic structure changes. It is only in the low temperature phase that a nonzero electric polarization appears. Similar behavior occurs in $TbMn_2O_5$. The first paper to study $TbMnO_3$ showed that a magnetic field can strongly influence the electric polarization e.g., in $TbMnO_3$ the polarization rotates by 90 degree when a critical magnetic field is applied along a certain direction [12]. In $TbMn_2O_5$ [13] the influence of an external field is even stronger, the polarization changes sign with field, and a field alternating between +1.5 and -1.5 Tesla leads to corresponding oscillations in the polarization. Since the discovery of these materials, a number of other type-II multiferroics with strong magnetoelectric coupling have been discovered and studied.

However, experimental development has shown that the conditions for coexistence of ferroelectricity and ferromagnetism are rarely met in single-phase materials. Alternative routes to producing multiferroics materials have therefore been explored, including composite systems made of a ferroelectric and a magnetic phase coupled to

each other via epitaxial strain. This work reports on local probe studies of magnetoelectric coupling in such a system, in which bismuth ferrite ($BiFeO_3$) and cobalt ferrite ($CoFe_2O_4$) play the role of the ferroelectric and magnetic phase respectively.

1.3 STRUCTURAL PROPERTIES OF $BiFeO_3$ AND $CoFe_2O_4$

1.3.1 PEROVSKITE STRUCTURE AND FERROELECTRICITY IN $BiFeO_3$

$BiFeO_3$ (BFO) has been intensively studied since 1960, due to the coexistence of antiferromagnetic and ferroelectric ordering in the bulk form of this material, with Neel temperature T_N ~ 643 K and Curie temperature T_C ~ 1103 K. In bulk single crystal form, the material shows a rhombohedrally distorted perovskite structure [14] with space group Rc3, where the oxygen octahedra are displaced along the [111] diagonal, inducing ferroelectric ordering [15, 16]. These octahedra are rotated along the [111] diagonal alternatively in one direction and the other, so that the real unit cell is rhombohedral and comprises two 'pseudocubic' perovskite unit cells see fig 1.1.

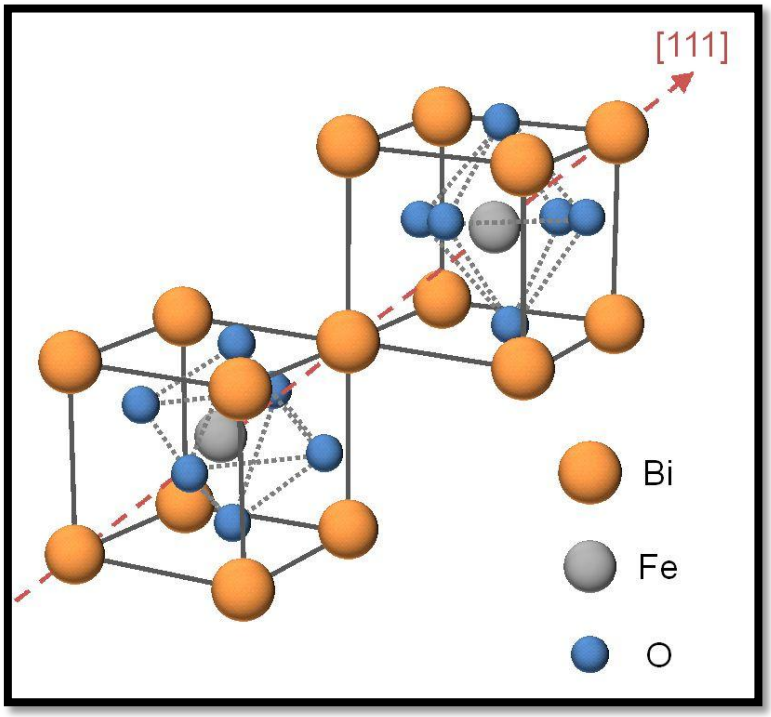

Figure 1.1 BFO rhombohedral unit cell.

Although initially some spread was observed in the measured ferroelectric polarization values due to varying crystal quality, there is now agreement that these values are some of the highest among ferroelectric materials, with a spontaneous polarization along the [111] direction of 100 $\mu C/cm^2$ measured by Lebeugle *et al.*[17] in

2007 in a BFO single crystal. Epitaxial thin films exhibit $P_s \sim 60\mu C/cm^2$ in the out-of-plane direction. These high polarization values, together with the high T_c and the absence of lead, make BFO an interesting candidate for industrial applications such as FeRAM.

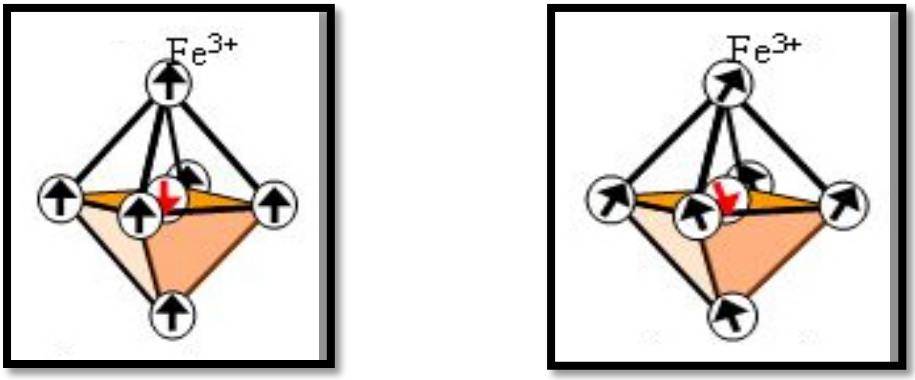

(a) Ideal (b) Canted

Figure 1.2 Ideal and canted G-type antiferromagnetism.

The Fe magnetic moments are ferromagnetically coupled within the (111) planes, with neighboring planes ordering anti-ferromagnetically, leading to G-type anti-ferromagnetism in the material as a whole. If the magnetic moments are oriented perpendicular to the [111] direction, the symmetry also permits a canting of the antiferromagnetic sublattices, resulting in Dzyaloshinskii-Moryia [18, 19] type weak ferromagnetism. Fig 1.2 shows the magnetic moment orientations in the ideal and canted G-type antiferromagnetism in BFO. In bulk BFO, an incommensurate spiral spin structure superimposed on the antiferromagnetic ordering leads to a cancellation of the macroscopic magnetization and inhibits the linear magnetoelectric effect. However, large magnetoelectric coupling has been reported in high quality epitaxial thin films.

In the framework of composite samples, the ferroelectric properties of BFO have led to evidence of strong magnetoelectric coupling in the work of Zavaliche *et al.* [20] raising a high interest in the $BiFeO_3$-$CoFe_2O_4$ system. However, the mechanism of this coupling is not yet fully understood, and in particular the role potentially played by the magnetic ordering in the BFO phase remains unclear.

1.3.2 PHASE DIAGRAM OF BFO

The phase diagram for the system Bi_2O_3/Fe_2O_3 has been graphed [21, 22, 23] and is shown in fig 1.3. $BiFeO_3$ is usually prepared from equal parts of Bi_2O_3 and Fe_2O_3, and

under high temperatures it can decompose back into these starting materials. Equation showing reaction,

$$Fe_2O_3 + Bi_2O_3 \rightarrow 2BiFeO_3$$

Bismuth ferrite is very likely to show parasitic phases that tend to nucleate at grain boundaries and impurities [24]. It has been studied that $BiFeO_3$ is in fact metastable in air, with optically visible impurity spots appearing well below the melting temperature [23, 25]. Impurities and oxygen vacancies are also important for thin films, because they are known to artificially enhance the remnant magnetization [26, 27].

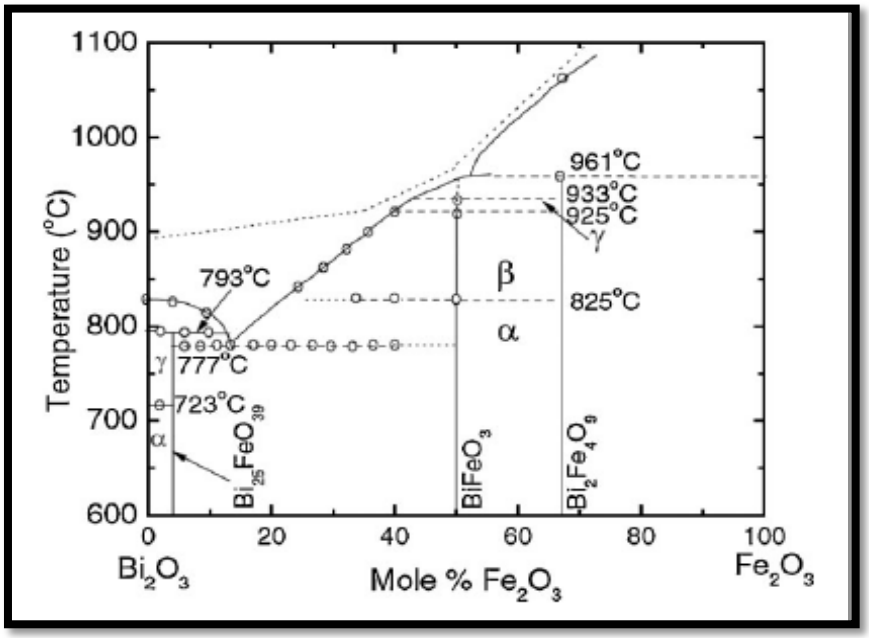

Figure 1.3 Compositional Phase diagram of $BiFeO_3$.

1.3.3 SPINEL STRUCTURE AND FERRIMAGNETISM IN $CoFe_2O_4$

$CoFe_2O_4$ (CFO) belongs to the spinel family, which is a group of compounds with a chemical formula of AB_2O_4, where A and B can be di-, tri- or tetravalent cations. The standard spinel structure consists of the A atoms occupying all of the tetrahedral coordination sites and the B atoms occupying all of the octahedral sites.

CFO has an inverse spinel structure, where the Co cations occupy one half of the octahedral coordination site, half the Fe cations occupy the other half of the octahedral coordination sites, and the other half of Fe cations occupy all the tetrahedral coordination sites. Practically all ferromagnets (and ferrimagnets) are magnetostrictives [28, 29]. At

room temperature, cobalt is the most magnetostrictive pure element. The crystal structure of CFO is shown in fig 1.4.

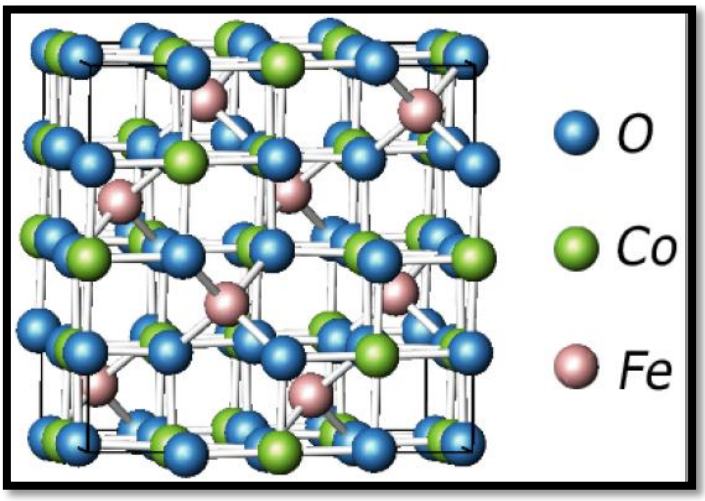

Figure 1.4 Inverse spinel structures in CFO.

A magnetostrictive material alters its shape as a result of two phenomena. First, the magnetic dipoles spin about their axis in order to reorient to match the external magnetic field. Second, the force felt by the external field causes the domain walls to migrate. These changes that occur on the level of individual dipoles and on the scale of domain walls both contribute to the shape change.

1.4 SYNTHESIS OF MULTIFERROIC THIN FILM BY DIFFERENT ROUTES

There are many techniques available for deposition of thin film on substrate. All of them having different advantages and disadvantages and can be used in different conditions. Some of them are discussed as follows,

- R F Sputtering
- Chemical Vapor Deposition
- Pulsed Laser Deposition
- Molecular Beam Epitaxy
- Spin Coating

1.4.1 R F SPUTTERING

Radio Frequency sputtering is a technique that is used to create thin films. Like direct current (DC) sputtering, this technique involves running an energetic wave through an inert gas to create positive ions. The target material, which will ultimately become the thin film coating, is struck by these ions and broken up into a fine spray that covers the substrate. During the sputtering process, the target material, substrate, and RF electrodes begin in a vacuum chamber. Next, the inert gas, which is usually argon, neon, or krypton, depending on the size of the target material's molecules, is directed into the chamber. The RF power source is then turned on, sending radio waves through the plasma to ionize the gas atoms. Once the ions begin to contact the target material, it is broken into small pieces that travel to the substrate and begin to form a coating.

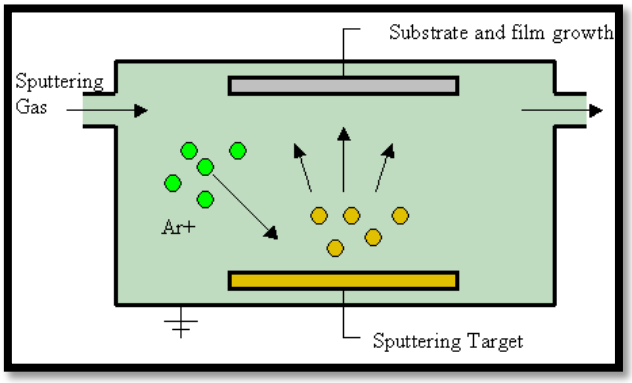

Figure 1.5 R-F Sputtering Technique.

RF sputtering uses radio waves instead of a direct electron current also RF systems use energy to remove the electrons from the gas atoms outer electron shells. Overheating is the most common issue with RF systems. The inert gas plasma in an RF system can be maintained at a much lower pressure of less than 15 mTorr. This allows for fewer collisions between the target material particles and the gas ions, creating a more direct pathway for the particles to travel to the substrate material. The combination of this decreased pressure, along with the method of using radio waves, makes RF sputtering ideal for target materials that have insulating qualities.

1.4.2 CHEMICAL VAPOR DEPOSITION (CVD)

Chemical vapor deposition (CVD) is a widely used materials-processing technology. The majority of its applications involve applying solid thin-film coatings to surfaces, but it is also used to produce high-purity bulk materials and powders, as well as

fabricating composite materials via infiltration techniques. It has been used to deposit a very wide range of materials.

CVD involves the flowing of a precursor gas or gases into a chamber containing one or more heated objects to be coated. Chemical reactions occur on and near the hot surfaces, resulting in the deposition of a thin film on the surface. This is accompanied by the production of chemical by-products that are exhausted out of the chamber along with unreacted precursor gases. As would be expected with the large variety of materials deposited and the wide range of applications, there are many variants of CVD. It is done in hot-wall reactors and cold-wall reactors, at sub-torr total pressures to above-atmospheric pressures, with and without carrier gases, and at temperatures typically ranging from 200-1600 °C. There are also a variety of enhanced CVD processes, which involve the use of plasmas, ions, photons, lasers, hot filaments, or combustion reactions to increase deposition rates and/or lower deposition temperatures. There are also many derivatives of CVD terminology, such as metal-organic chemical vapor deposition (MOCVD) or less commonly, organo-metallic chemical vapor deposition (OMCVD), which are sometimes used to note the class of molecules used in the deposition process.

CVD has a number of advantages as a method for depositing thin films. One of the primary advantages is that CVD films are generally quite conformal, i.e., that the film thickness on the sidewalls of features is comparable to the thickness on the top. This means that films can be applied to elaborately shaped pieces, including the insides and undersides of features, and that high-aspect ratio holes and other features can be completely filled.

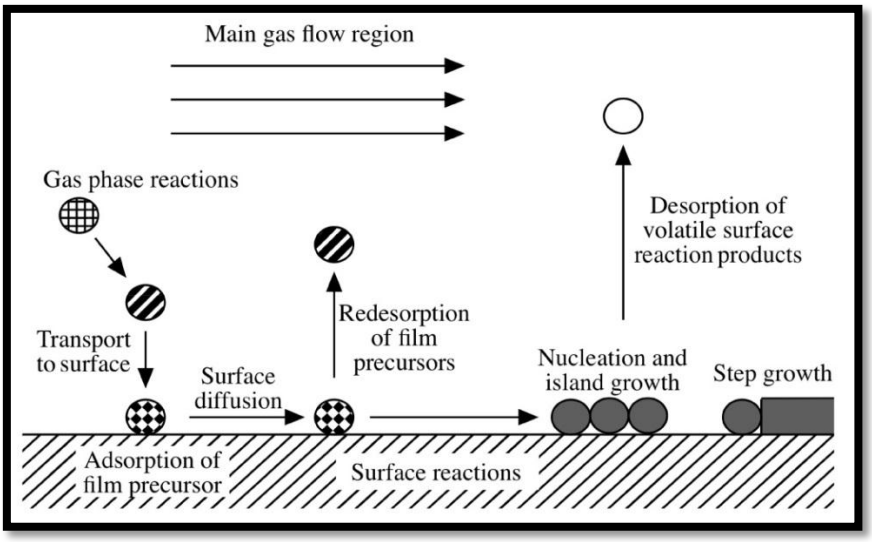

Figure 1.6 Schematic of CVD.

Another advantage of CVD is that, in addition to the wide variety of materials that can be deposited, they can be deposited with very high purity. This results from the relative ease with which impurities are removed from gaseous precursors using distillation techniques. Other advantages include relatively high deposition rates, and the fact that CVD doesn't require high vacuum.

1.4.3 PULSED LASER DEPOSITION (PLD)

Conceptually and experimentally, pulsed laser deposition is an extremely simple technique, probably the simplest among all thin film growth techniques shown in fig 1.7. It consists of a target holder and a substrate holder housed in a vacuum chamber. A high-power laser is used as an external energy source to vaporize materials and to deposit thin films. A set of optical components is used to focus and raster the laser beam over the target surface. The decoupling of the vacuum hardware and the evaporation power source makes this technique so flexible that it is easily adaptable to different operational modes without the constraints imposed by the use of internally powered evaporation sources. PLD demonstrated to be a versatile technique for thin film processing with a high diversity of structural and morphological characteristics [30, 31]. Many independent parameters can be changed under control in order to select the optimum deposition. Growing thin films by PLD has numerous advantages, such as:

- The laser source is placed outside the deposition chamber offering increased flexibility in handling the material, laying out the geometrical setup, and adjusting deposition parameters.
- Multistructures can be easy synthesized.
- Laser pulses make possible to control the growth rate of the coating very accurately (down to a few fractions of Å).
- Stoichiometry of coating materials generally coincides with that of the target even for complex, highly unstable compounds.

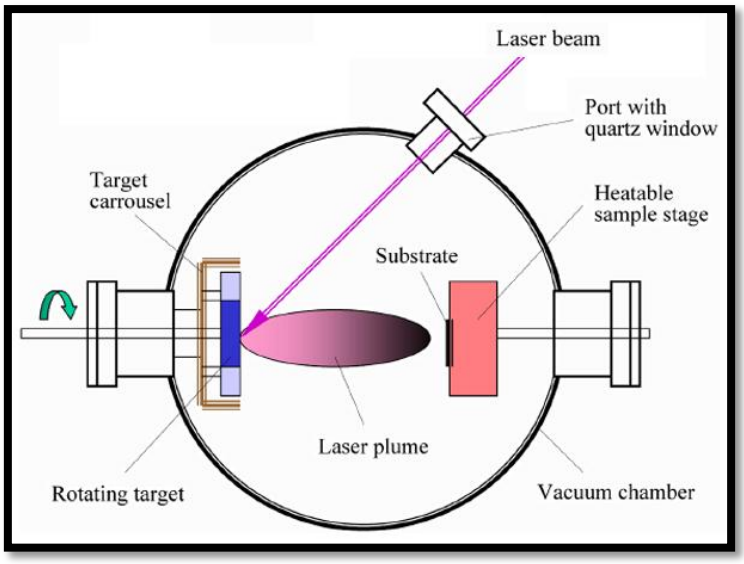

Figure 1.7 Pulsed laser deposition technique.

1.4.4 MOLECULAR BEAM EPITAXY (MBE)

Molecular beam epitaxy (MBE) is one of several methods of depositing single crystals. Molecular beam epitaxy is a technique for epitaxial growth via the interaction of one or several molecular or atomic beams that occurs on a surface of a heated crystalline substrate. In fig 1.8 a scheme of a typical MBE system is shown. The solid sources materials are placed in evaporation cells to provide an angular distribution of atoms or molecules in a beam. The substrate is heated to the necessary temperature and, when needed, continuously rotated to improve the growth homogeneity. Some of the characteristics of MBE are as follows,

- Low growth rate of ~ 1 monolayer (lattice plane) per sec.
- Low growth temperature.
- Smooth growth surface with steps of atomic height and large flat terraces.
- Precise control of surface composition and morphology.
- Abrupt variation of chemical composition at interfaces.
- In-situ control of crystal growth at the atomic level.

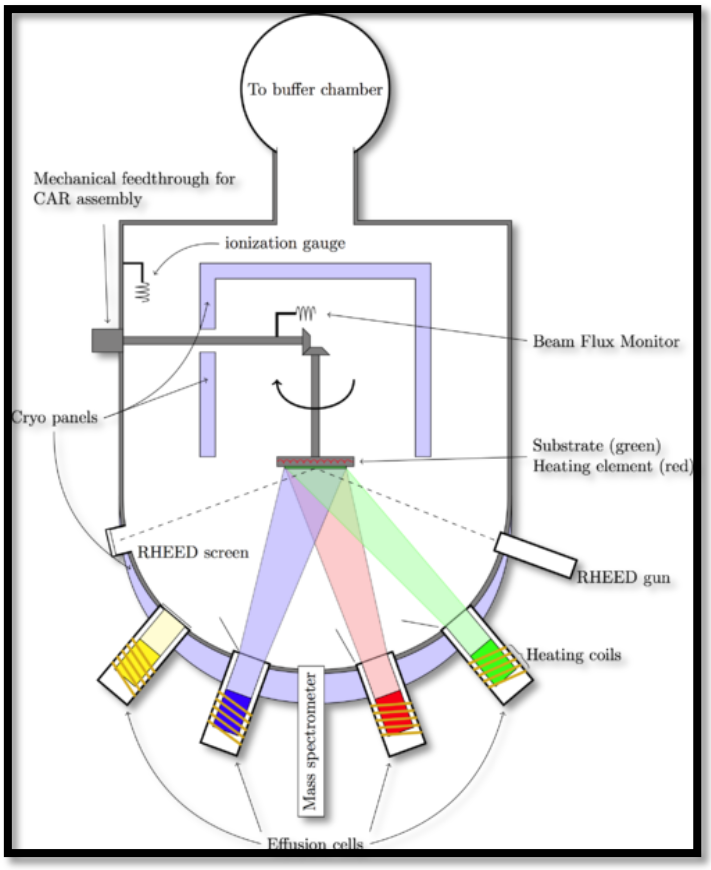

Figure 1.8 Schematic of MBE System.

1.4.5 SPIN COATING

Spin coating has been used for deposition of thin film. Spin coating is a technique used to apply uniform film to flat substrate. The platform is such that there is small hole at the center of platform which is connected to vacuum pump. When a flat substrate is kept on platform substrate, it close the small hole and then vacuum is created inside, so that substrate stick to the platform and when platform rotates only solution could move on the substrate. Rotation is continued while the fluid spins off the edges of the substrate so that desired thickness of the film is achieved. Higher the angular speed of spinning, thinner the film. The thickness also depends on the concentration of the solution and solvent.

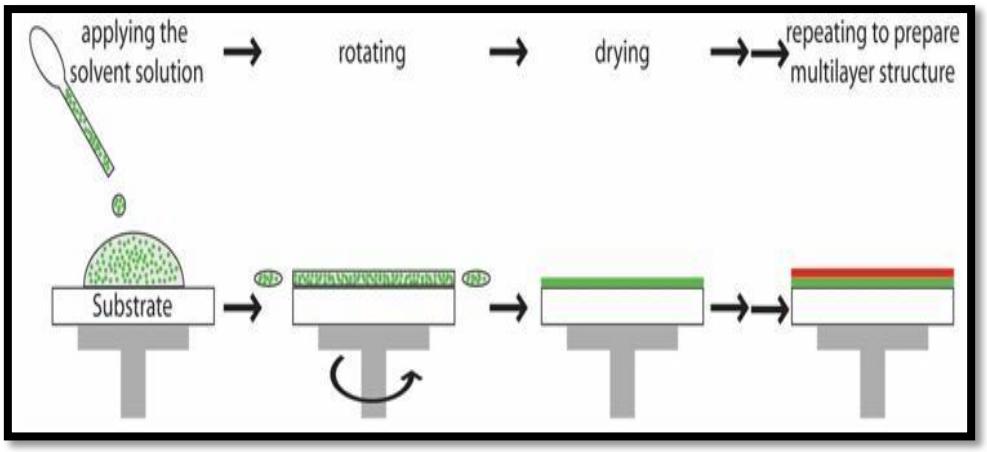

Figure 1.9 Spin coating technique.

This process involves a small amount of solution onto center of a substrate and then spinning substrate putting at high speed. Final film thickness and other properties will depend on nature of solution (viscosity, drying rate, surface tension etc.) and parameters chosen for spin process such as rpm and spin time. Spin coating process involve 4 stages as shown in below fig 1.9. Dropping or applying sol on substrate, rotating, drying and repeating process to prepare multilayer structure.

CHAPTER 2

LITERATURE REVIEW

Many researchers, scientists and various groups are actively involved in the study and synthesis of $BiFeO_3$-AFe_2O_4 composite thin films via different techniques e.g. (radio frequency sputtering, chemical vapor deposition, pulse laser deposition method, etc). In comparison to the above said methods, synthesis using sol gel processing has many advantages like easy setup, cheaper, flexible control of the phase constituents and dopants, and large area coverage etc. The current literature review summarizes some important work carried out on $BiFeO_3$-AFe_2O_4 thin films by different technique.

Liu *et al.* in 2005 [32] studied and presented the novel mixed spinel perovskite composites of x $CoFe_2O_4$ $(1-x)$ $BiFeO_3$ (x = 0.1, 0.2, 0.3, 0.4) prepared by sol–gel technique. TEM results showed that the composites consisted of spinel $CoFe_2O_4$ and perovskite $BiFeO_3$ after annealing at a temperature higher than 400 ^{0}C, and the crystal size ranges found to vary from 20 to 80 nm. The composites with composition 0.3 $CoFe_2O_4$- 0.7 $BiFeO_3$ annealed at 700 ^{0}C exhibited the largest coercivity (H_c) of 1351 Oe and the optimal squareness (M_r/M_s) of 54%. The saturation magnetization (M_s) and coercivity (H_c) increase drastically with the increase of $CoFe_2O_4$ concentration in the composites when annealed at 700 ^{0}C.

Zhou *et al.* in 2006 [33] developed multiferroic laminated composites of $Pb(Zr_{0.52}Ti_{0.48})O_3$(PZT)/$CoFe_2O_4$ (CFO) prepared by conventional ceramic processing. The dielectric behavior of such a sandwiched ceramic was dominated by the relative thickness of the different layers because of the high dielectric constant of the PZT layer and the low dielectric constant of the CFO layer. The magnetoelectric behaviors were strongly dependent on the relative thickness of the CFO layer, dc magnetic field, ac magnetic frequency, and the angle between the magnetic field and polarization direction. The maximal magnetoelectric induced voltage coefficient of the composites reaches up to about 27 mV/Oe, close to what was reported previously.

Lee *et al.* in 2006 [34] worked on growth of multiferroics $BiFeO_3$ thin film by sol gel method. He spin-coated $BiFeO_3$ thin films onto Pt(1 1 1)/Ti/SiO_2/Si(1 0 0) substrates. The Bragg factors RB and RF were 8.79% and 4.85%, respectively. Scanning electron microscope (SEM) pictures revealed that the matrix is uniform and no segregation of

impurity phase was detected. Auger electron spectroscopy (AES) analysis indicated that the sample is chemically homogeneous with Bi/Fe atomic percent ratio being close to 1. Images of atomic force microscopy (AFM) show that their root-mean squared and average values of the surface roughness of the film were 34.3 and 27.3 Å respectively. The differential scanning calorimetry (DSC) curve indicates a phase transition at a temperature of 354 ^{0}C. The film shows well-saturated weak ferromagnetic hysteresis loop with maximum magnetic field of 10 kOe at room temperature.

Zhong *et al.* in 2007 [35] prepared multiferroic x $Bi_{3.15}Nd_{0.8}5Ti_3O_{12}$ – $(1-x)$ $CoFe_2O_4$ composite thin films with x = 0.5, 0.6, and 0.7 were fabricated on Pt/Ti/SiO_2/Si (100) substrates by a chemical solution deposition technique. X-ray diffraction shows that there are no other phases but bismuth-layered perovskite $Bi_{3.15}Nd_{0.8}5Ti_3O_{12}$ and spinal $CoFe_2O_4$ phases in the films. Scanning electron microscopy reveals that $CoFe_2O_4$ aggregates locally into nanoparticles and embeds in the $Bi_{3.15}Nd_{0.8}5Ti_3O_{12}$ matrix. The composite films exhibit both good ferroelectric and magnetic properties at room temperature, as well as distinct magnetoelectric coupling behaviors, which are comparable with those of multiferroic composite films with conventional Pb-based ferroelectric as a ferroelectric component.

Roy *et al.* in 2007 [36] worked on a hybrid sol-gel route and synthesized $CoFe_2O_4$/ $Pb_{0.85}La_{0.15}TiO_3$ (CFO/PLT) composite thin films on platinized silicon substrates. At room temperature, these composite films exhibit both polarizations as well as magnetization hysteresis loops. As compared to pure PLT thin films, the PLT-CFO composite films exhibit lower saturation (35μC/cm^2) and remnant polarizations (10μC/cm^2) with reduced coercive fields.

Yasui *et al.*in 2008 [37] worked on enhancement of ferroelectric and magnetic properties in $BiFeO_3$ films by small amount of cobalt addition. Both the ferroelectric and magnetic properties of polycrystalline $BiFeO_3$ films fabricated by chemical solution deposition were enhanced by adding small amounts of cobalt. Addition of 3 at.% cobalt to $BiFeO_3$ films increased the remnant polarization from 49 to 72 μC/cm^2 and decreased the electric coercive field from 0.54 to 0.44 MV/cm. The ferroelectricity degraded when the cobalt concentration exceeded 9 at.% due to the formation of the secondary phases of Bi_2Pt. The saturation magnetization was drastically enhanced by the addition of cobalt up to 12 at. %. The saturation magnetization decreased when the cobalt content exceeded 15 at. %, thereby, attributing to the formation of a nonmagnetic secondary phase of Bi_2Pt. It is

concluded that both ferroelectric and magnetic properties were enhanced, provided only small amount of cobalt were added to the films.

Zheng *et al.* in 2008 [38] developed a magnetoelectric heterostructure with desired ferroelectric and magnetic properties, a heterostructure consisting of $BiFeO_3$(BFO)/$CoFe_2O_4$(CFO) layers has been grown on $SrRuO_3$ buffered Pt/TiO_2/SiO_2/Si substrate by R-F sputtering. Grain growth of the CFO phase was enhanced on top of the BFO layer. The heterostructure exhibits both ferroelectric and magnetic behaviors at room temperature. Its remnant polarization is measured to be (146 C/cm^2) and the coercive field (2*Ec* is 1803 kV/cm), while the saturation magnetization (2*Ms* is 140 emu/cm^3) and the coercive field (2*H*c is 2.7 kOe.)

Muralidharan *et al.* in 2008 [39] synthesized self-assembled (0.65 $BiFeO_3$ - 0.35 $CoFe_2O_4$) (BFO-CFO) nanostructures were deposited on $SrTiO_3$ (001) and (111) substrates by pulsed laser deposition at various temperatures from 500 to 800 ^{0}C. The crystal phases and the lattice strain for the two different substrate orientations have been determined and compared. The films grow epitaxial on both substrates but separation of the spinel and perovskite crystallites, without parasitic phases, is only obtained for growth temperatures of around 600–650 ^{0}C. The BFO crystallites are out-of-plane expanded on STO (001), whereas they are almost relaxed on (111). It is concluded that interfacial stress dominates the elastic properties of CFO crystallites and thus it may play a fundamental on the interface magnetoelectric coupling in these nanocomposites.

Wu *et al.* in 2009 [40] done research work on Lead-free bilayered multiferroic thin films consisting of $BiFeO_3$ (BFO) and $CoFe_2O_4$ (CFO) layers with different thicknesses were grown on $SrRuO_3$-coated Pt/TiO_2/SiO_2/Si substrates by radio frequency sputtering. The effects of constituent layer thicknesses on the ferroelectric and magnetic behaviour have been studied. BFO (220 nm)/CFO (30 nm) bilayered thin film demonstrated much improved ferroelectric and ferromagnetic behavior (2*Pr* = 144.2 C/cm^2), 2*Ec* = 778.0 kV/cm, *Ms* = 61.20 emu/cm^3, and *Hc* = 200.80 Oe as compared to those of the single layer BFO thin film. The dielectric behavior and conductivity of BFO (220 nm)/CFO (30 nm) bilayered thin film were investigated as a function of temperature.

Yan *et al*. in 2009[41] studied the ferroelectric, ferromagnetic, and magnetoelectric (ME) properties of self-assembled epitaxial $BiFeO_3$–$CoFe_2O_4$ (BFO–CFO) nanostructure composite thin films deposited on (001), (110), and (111) $SrTiO_3$ (STO) single crystal substrates. These various properties are shown to depend on orientation. The maximum values of the relative dielectric constant, saturation polarization, longitudinal piezoelectric

coefficient, saturation magnetization, and ME coefficient at room temperature were 143, 86 μm/cm^2, 50 pm/V, 400 emu/cc, and 20 mV/cm Oe, respectively.

Zhu *et al.* in 2010 [42] reported multiferroic $BiFeO_3$-$CoFe_2O_4$ (BFO-CFO) double- layer thin film which has been deposited on platinized silicon substrate by pulsed-laser deposition. The BFO and CFO thin layers are deposited at 450 and 600 °C respectively. Dielectric constant and loss of the BFO-CFO films are of around BFO 60 and 0.06 respectively, changing little with increasing the frequency. The leakage current density is about 10^{-6} A/cm^2 under the field of 100 kV/cm. BFO-CFO thin films exhibit good ferromagnetic properties with the saturation magnetization of 120 emu/cm^3.

Chen *et al.* in 2010 [43] reported $CoFe_2O_4$– $Pb(Zr_{0.52}Ti_{0.48})O_3$ (CFO–PZT) multiferroic composite thick films sandwiched by PZT composite films prepared by sol–gel processing and spin-coating technique. Deeply buried $CoFe_2O_4$ spinel ferrite phase could not be detected in X-ray diffraction pattern. In addition, EDX results also detected $CoFe_2O_4$ composite from the cross section of thick films but were not observed on its surface. The structure of CFO–PZT composite thick films could be made denser by introducing enough PZT sol–gel for infiltration after each coated, composite layer and ferroelectric and dielectric properties of composite thick films were hence, improved remarkably with stable magnetic properties.

Stern *et al.* in 2011 [44] prepared epitaxial thin films of $BiFeO_3$- $CoFe_2O_4$ composite on spinel $MgAl_2O_4$ substrates with a (001) orientation. The composite formed an intriguing nanogrid structure where perovskite $BiFeO_3$ forms linear mounds embedded in a matrix of spinel $CoFe_2O_4$. The structure makes a stark distinction with similar composite films on (001) perovskite $SrTiO_3$ substrates where $CoFe_2O_4$ forms nanopillars surrounded by a $BiFeO_3$ matrix. This result shows the interface between the film and the substrate that plays a determining role.

Aimon *et al.* in 2012 [45] developed a $BiFeO_3$/ $CoFe_2O_4$ (BFO/CFO) nanocomposite which was grown on $SrTiO_3$ by pulsed laser deposition using a combinatorial method in which $Bi_{1.2}FeO_3$ and $CoFe_2O_4$ targets are alternately ablated. The films had the same vertically nanostructure morphology as thin films prepared by ablation of a single target, consisting of epitaxial $CoFe_2O_4$ pillars in a $BiFeO_3$ matrix. In a series of samples synthesized with a compositional spread, the out-of-plane magnetic anisotropy and the out-of-plane compressive strain of the $CoFe_2O_4$ pillars increased with decreasing volume fraction, and the anisotropy agreed with the value predicted from the strain state and

magnetoelastic coefficients of $CoFe_2O_4$. These results show the dominant effect of magnetoelastic anisotropy in determining the magnetic hysteresis of the nanocomposite.

Sone *et al* .in 2012 [46] worked on $BiFeO_3$-$CoFe_2O_4$ composite thin films which were formed on Pt/Ti/SiO_2/Si (100) substrates by chemical solution deposition from a mixed precursor solution. $BiFeO_3$-$CoFe_2O_4$ composite films exhibited the same ferroelectric switching charge as $BiFeO_3$ thin films, although a larger applied electric field was necessary. However, the magnetic properties were significantly improved by incorporation of $CoFe_2O_4$ nanoparticles into $BiFeO_3$; a saturated magnetization of 80 emu/cm^3 and a magnetic coercive field of 450 Oe were attained at 300 K. Furthermore, the composite films did not show superparamagnetic behavior in zero-field-cooling and field-cooling measurements, which suggest that the thermal fluctuation of $CoFe_2O_4$ nanoparticles was suppressed by exchange coupling with $BiFeO_3$.

Li *et al*. in 2012 [47] studied the growth mechanism of a $BiFeO_3$ layer deposited on self-assembled (0.65) $BiFeO_3$-(0.35) $CoFe_2O_4$ (BFO-CFO) composite thin films. Epitaxial and self-assembled BFO-CFO thin films were deposited on $SrTiO_3$ (111) substrates by pulsed laser deposition and used as a seed layer for the deposition of an additional BFO layer. X-ray line scans showed the heterostructures were highly epitaxial. Cross-sectional scanning electron microscopy and focused ion beam images revealed the top BFO layer grew preferentially from BFO nanopillarsin the BFO-CFO thin films, demonstrating controlled growth. The multiferroic properties of this new nanostructure were then studied.

CHAPTER 3

EXPERIMENTAL METHOD

Thin film coating was the earliest and so far one of the most important application of sol-gel technology. Recent year are marked by growing interest in sol gel processed film in new areas, in particular in microelectronics. This is mainly due to intensively developing application and preparation of ferroelectric film for non-volatile matter and so on.

Spin coating is one of the techniques for thin film deposition from liquid precursors used in microelectronics industry. A large variety of high performance systems, providing coating of photoresists, polyimides and spin-on-glasses are available from manufacturers. Thus dipping is frequently used in sol-gel film preparation, but it has number of limitation like double side coating, non- uniformity on wafer edge, rather high contamination level (solution is polluted by particles from substrate and the container walls which are then recoated from the solution surface into the growing film; the solution applied cannot be filtered just before use) and some other. Therefore practical application of sol-gel thin film route at least for microelectronic applications is connected with the spin coating process.

3.1 SOL-GEL PREPARATION

The sol-gel process may be described as “Formation of oxide network through polycondensation reactions of a molecular precursor in a liquid.” Sol is a stable dispersion of colloidal particles or polymers in a solvent. A gel consists of a three dimensional continuous network, which encloses a liquid phase, in a colloidal gel, the network is built from agglomeration of colloidal particles fig 3.1. The idea behind sol-gel synthesis is to “dissolve” the compound in a liquid in order to bring it back as a solid in a controlled manner. Multi component compounds may be prepared with a controlled stoichiometry by mixing sols of different compounds. The sol-gel method prevents the problems with co-precipitation, which may be inhomogeneous, be a gelation reaction. It enables mixing at an atomic level. It results in small particles, which are easily sinterable.

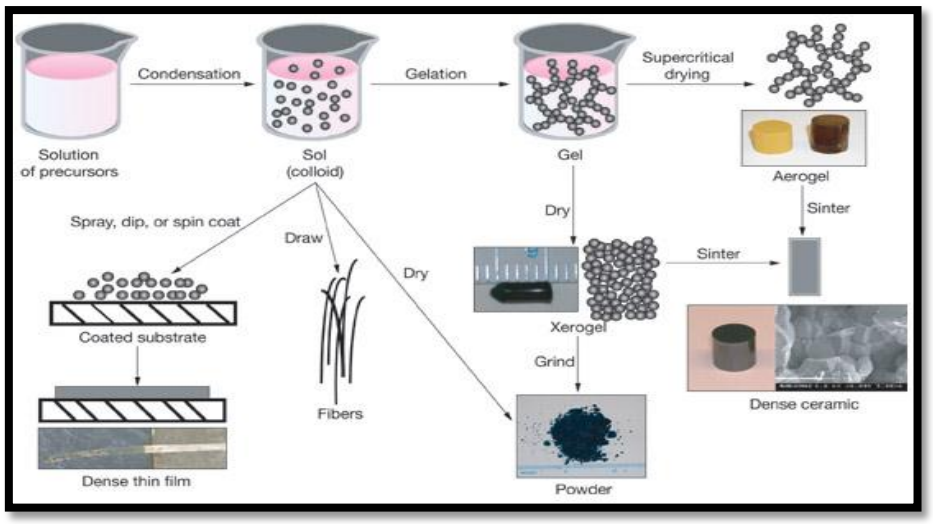

Figure 3.1 Schematic of Sol-Gel Technique

The multiferroic composite thin films were prepared by sol-gel method and spin-coating technique. A 0.2 M BFO precursor solution was prepared by dissolving bismuth nitrate pentahydrate (Bi $(NO_3)_3.5H_2O$) and iron nitrate nonahydrate (Fe $(NO_3)_3.9H_2O$) with the molar ratio of 1:1 into 2-methoxyethanol and 10 mol % excess bismuth nitrate was used to compensate for the volatile Bi loss during annealing process. Also, cobalt nitrate hexahydrate (Co $(NO_3)_2.6H_2O$) and iron nitrate nonahydrate (Fe $(NO_3)_3.9H_2O$) were dissolved in 2-methoxyethanol with molar ratio of 1:2 to derive 0.2M CFO precursor solution. Then both precursor solutions of BFO and CFO were mixed together with volume ratio of BFO/CFO (x = 0, 0.1), heated and stirred continuously at 70 °C for 1 hours to get a well-mixed BFO-CFO gel solution. The mixed solution was spin coated onto indium tin oxide coated (ITO) glass substrate at 3000 rpm for 40 sec. and subsequently baked at 300 °C for 5 min. Finally the thin films were obtained by repeating this spin-coating-baking-annealing process twice. The films were annealed at 650 °C for 30 min in ambient atmosphere., Phase analysis of the composite thin films were analyzed by X-ray diffraction (XRD) using CuKα radiation (λ = 1.54178 Å) (Philips X-pert PRO). Thickness of the film was measured by profilometer. Surface morphology of the films were studied by Atomic force microscopy AFM (NT-MDT SOLVER NEXT).The compositional analysis of the composite thin films was performed using energy dispersive x-ray spectroscopy (EDX). For electrical measurements, the Au dots of 0.8 mm were deposited using the mask on the film by sputtering technique. Ferroelectric properties were measured using HP 4192A impedance analyzer and using a ferroelectric tester (Radiant Precision Premier II Technology) respectively. Magnetization hysteresis loops

were measured using a superconducting quantum interference device (SQUID) (Quantum Design's MPMS XL7).

Prior to spinning, several of the substrate were cleaned or etched for 5 minutes using ultrasonic cleaning device. Etching or cleaning substrate surface has been done alternately by soap solution, acetone and distilled water. Then immediately after spin coating, spin coated substrate is baked on furnace for 2 min at 300 ^{0}C to gelate the solution. And finally sample is annealed at 650 ^{0}C for 40 minutes in furnace. And finally different characterization of film is done.

3.2 EXPERIMENTAL FLOW CHART

Flow chart of experimental method fig 3.2 is as follows,

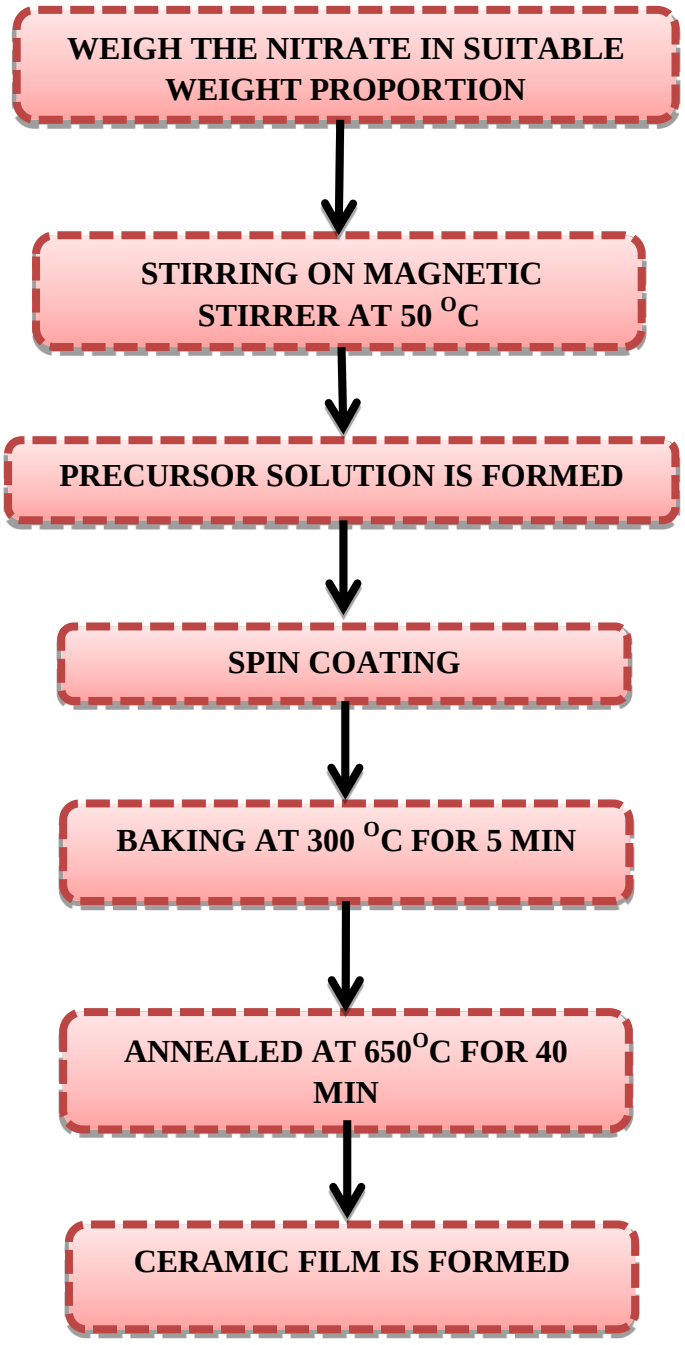

Figure 3.2 Flow chart of experimental method.

3.3 CHARACTERIZATION TECHNIQUES

3.3.1 X-RAY DIFFRACTION (XRD)

X-ray Diffraction (XRD) is a rapid analytical technique used for phase identification of a crystalline material and can provide information of unit cell dimensions. Schematic diagram of X-ray Diffraction instrument is shown in fig 3.3. X-ray diffraction is basically based on constructive interference of monochromatic X-rays and a crystalline sample. These X-rays are generated by a cathode ray tube, filtered to produce monochromatic radiation, collimated to concentrate, and directed toward the sample.

Figure 3.3 X-ray Diffraction instrument.

The interaction of the incident rays with the sample produces constructive interference (and a diffracted ray) when conditions satisfy Bragg's Law ($n\times\lambda = 2\times d\times\sin\theta$) as shown in fig 3.4 [48]. This Bragg's law relates the wavelength of electromagnetic radiation to the diffraction angle and the lattice spacing in a crystalline sample. These diffracted X-rays are then detected, processed and counted. By scanning the sample through a range of 2θ angles, all possible diffraction direction of lattice obtained due to the random orientation of the powder material. Conversion of the diffraction peaks to d-spacing allows identification of the mineral because each material has a set of unique d-spacing. Typically, this is achieved by comparison of d-spacing with standard reference patterns.

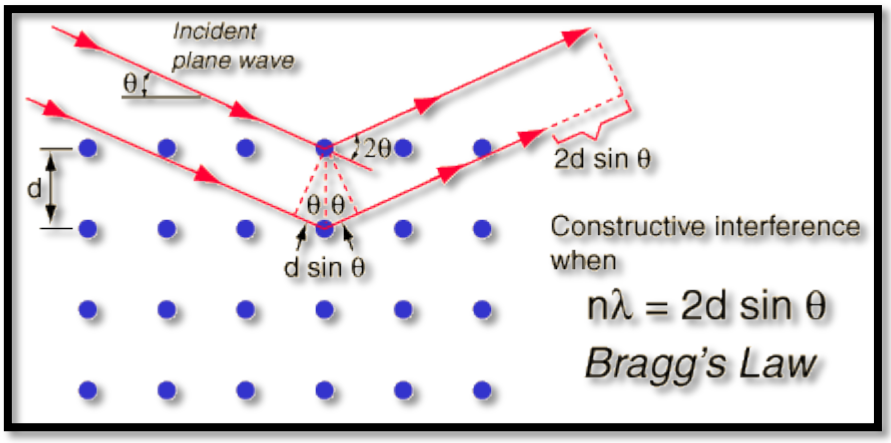

Figure 3.4 Bragg's Law.

A traditional X-ray diffractometer as shown in fig 3.3 consists of three basic components: An X-ray tube, a sample holder, and an X-ray detector. X-rays are generated in a cathode ray tube by heating a filament to produce electrons, accelerating the electrons towards a target by applying a voltage, and bombarding the target material with electrons. When electrons have sufficient energy to dislodge inner shell electrons of the target material, characteristic X-ray spectra are produced. These spectra consist of several components, the most common being K_α and K_β. The specific wavelength is characteristic of the target material (Cu, Fe, Mo, and Cr).

Copper is the most common target material for single-crystal diffraction, with CuKα radiation equals 1.541 Å. These X-rays are collimated and directed onto sample. The collimation is performed using cones or collimators (multi-leaf collimator or iris diaphragms) that are attached directly in front of X-ray tube. As the sample and detector are rotated, the intensity of the reflected X-rays is recorded. When the geometry of the incident X-rays impinging the sample satisfies the Bragg equation, constructive interference occurs and a peak in intensity occurs. A detector records and processes this X-ray signal and converts the signal to a count rate which is then output to a device such as a printer or computer monitor. Our phase analysis of the composite thin films were done by X-ray diffraction (XRD) using CuKα radiation (λ = 1.54178 Å) (Philips X-pert PRO).

3.3.2 ATOMIC FORCE MICROSCOPY

The atomic force microscope (AFM) was invented by Binning *et al.* in 1986 [49]. The AFM measures the forces acting between a fine tip and a sample. The tip is attached to the free end of a cantilever and is brought very close to a surface. Attractive or

repulsive forces resulting from interactions between the tip and the surface will cause a positive or negative bending of the cantilever. The bending is detected by means of a laser beam, which is reflected from the back side of the cantilever. Fig 3.5 shows the basic concept of AFM. Surface morphology of the films were studied by Atomic force microscopy (AFM) model (NT-MDT SOLVER NEXT).

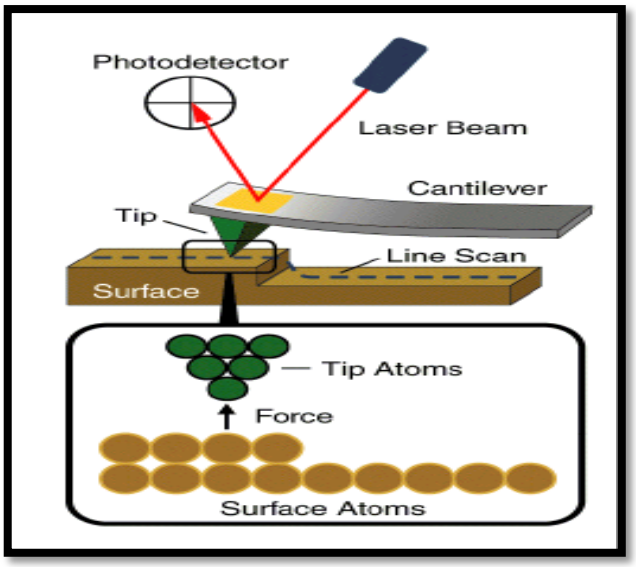

Figure 3.5 Principal of working of AFM.

AFM MODES OF OPERATION

Because of AFM's versatility, it has been applied to a large number of research topics. The Atomic Force Microscope has also gone through many modifications for specific application requirements.

- **CONTACT MODE**

  The first and foremost mode of operation, contact mode is widely used. As the tip is raster-scanned across the surface, it is deflected as it moves over the surface corrugation. In constant force mode, the tip is constantly adjusted to maintain a constant deflection, and therefore constant height above the surface. It is this adjustment that is displayed as data. However, the ability to track the surface in this manner is limited by the feedback circuit. Sometimes the tip is allowed to scan without this adjustment, and one measures only the deflection. This is useful for small, high-speed atomic resolution scans, and is known as variable-deflection mode.

Because the tip is in hard contact with the surface, the stiffness of the lever needs to be less that of the effective spring constant holding atoms together, which is on the order of 1 - 10 nN/nm. Most contact mode levers have a spring constant of < 1N/m.

- **LATERAL FORCE MICROSCOPY (LFM)**

LFM measures frictional forces on a surface. By measuring the "twist" of the cantilever, rather than merely its deflection, one can qualitatively determine areas of higher and lower friction.

- **NONCONTACT MODE**

Noncontact mode belongs to a family of AC modes, which refers to the use of an oscillating cantilever. A stiff cantilever is oscillated in the attractive regime, meaning that the tip is quite close to the sample, but not touching it (hence, "noncontact"). The forces between the tip and sample are quite low, on the order of pN (10^{-12} N). The detection scheme is based on measuring changes to the resonant frequency or amplitude of the cantilever.

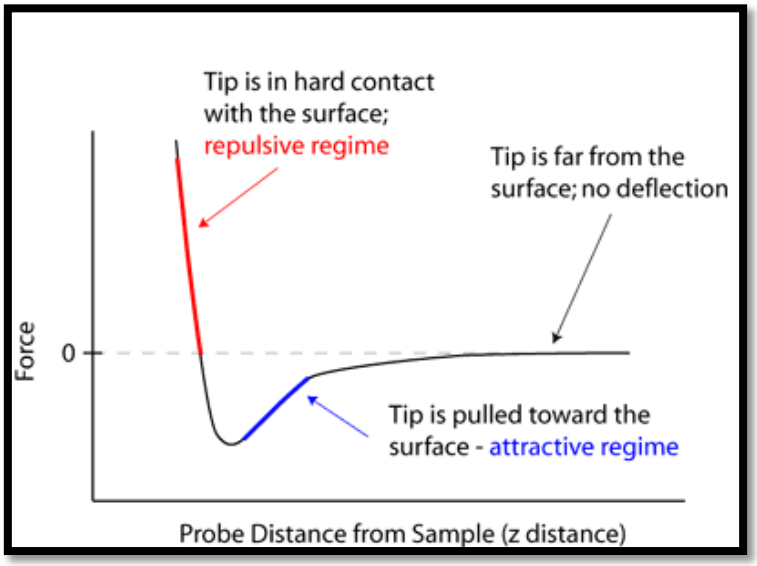

Figure 3.6 Diagram showing different modes of operation.

3.3.3 SUPERCONDUCTING QUANTUM INTERFACE DEVICE (SQUID)

SQUID magnetometer is one of the most effective and sensitive ways of measuring magnetic properties. In particular, it is the only method which allows to directly determining the overall magnetic moment of a sample in absolute units. When the sample is moved up and down it produces an alternating magnetic flux in the pick-up coil .The magnetic signal of the sample is obtained via a superconducting pick-up coil

with 4 windings. This coil is, together with a SQUID antenna (red in fig 3.7), part of a whole superconducting circuit transferring the magnetic flux from the sample to an RF-SQUID device which is located away from the sample in the liquid helium bath. This device acts as a magnetic flux-to-voltage converter (blue in fig 3.7). This voltage is then amplified and read out by the magnetometer's electronics (green in fig 3.7). Magnetization hysteresis (*M-H*) loops were measured using a superconducting quantum interference device (SQUID) (Quantum Design's MPMS XL7).

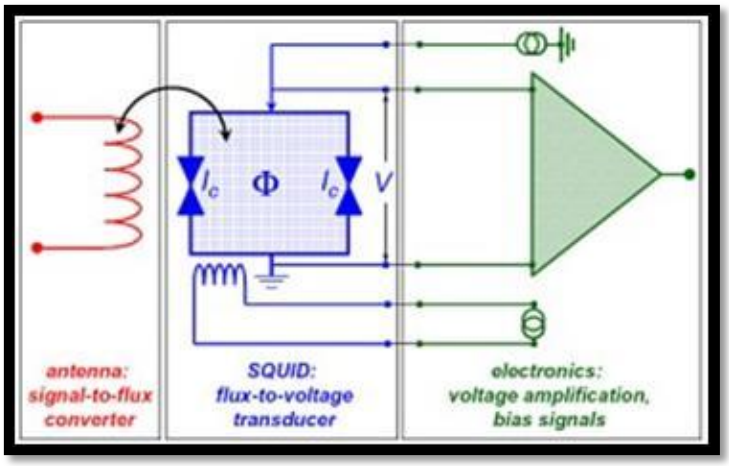

Figure 3.7 Circuit diagram of SQUID.

3.3.4 POLARIZATION FIELD (P-E LOOP) MEASUREMENT

A P-E loop for a device is a plot of the charge or polarization (P) developed, against the field applied to that device (E) at a given frequency. The significance of this measurement can be more easily understood by examining the P-E loops for some simple linear devices. The P-E loop for an ideal linear capacitor is a straight line whose gradient is proportional to the capacitance fig 3.8(a). This is because for an ideal capacitor the current leads the voltage by 90 degrees, and therefore the charge (the integral of the current with time) is in phase with the voltage.

For an ideal resistor the current and voltage are in phase and so the P-E loop is a circle with the center at the origin fig 3.8(b). If these two components are combined in parallel we get the P-E loop in fig 3.8(c) which is in effect a loss capacitor, where the area within the loop is proportional to the loss tangent of the device, and the slope proportional to the capacitance. If we now consider less ideal devices such as non-linear ferroelectric materials we would get a P-E loop such as fig 3.8(d). The nature of piezoelectric materials is that a change in its polarization state is coupled with a piezoelectric strain,

which is the most used functional response of the material. For electrical measurements, the Au dots of 0.8 mm were deposited using the mask on the film by sputtering technique. Ferroelectric properties were measured using a ferroelectric tester (Radiant Precision Premier II Technology).

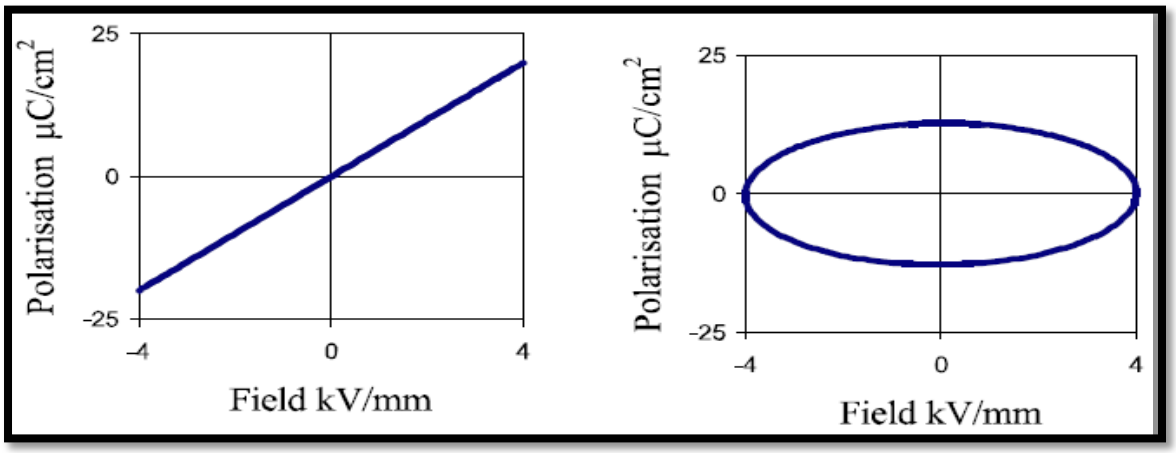

Figure 3.8(a) Figure 3.8(b)

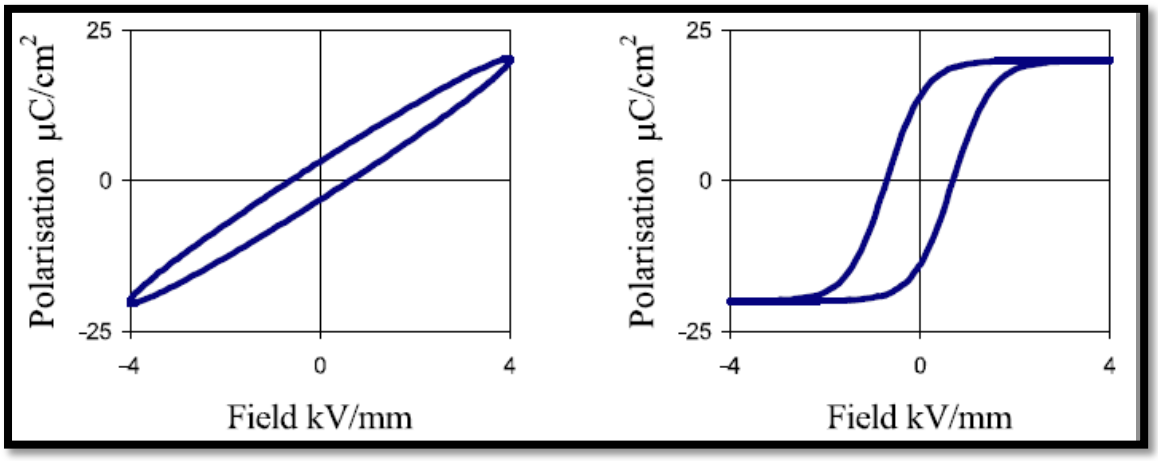

Figure 3.8(c) Figure 3.8(d)

Figure 3.8 Schematic of P-E loop for different devices.

3.3.5 ENERGY DISPERSIVE X-RAY SPECTROSCOPY (EDS)

Energy-dispersive X-ray spectroscopy (EDS, EDX, or XEDS) is an analytical technique used for the elemental analysis or chemical characterization of a sample. Energy Dispersive X-Ray Spectroscopy (EDS or EDX) is a chemical microanalysis technique used in conjunction with scanning electron microscopy (SEM). The EDS technique detects X-rays emitted from the sample during bombardment by an electron beam to characterize the elemental composition of the analyzed volume. Features or phases as small as 1 μm or less can be analyzed.

When the sample is bombarded by the SEM's electron beam, electrons are ejected from the atoms comprising the sample's surface. The resulting electron vacancies are filled by electrons from a higher state, and an X-ray is emitted to balance the energy difference between the two electron states. The X-ray energy is characteristic of the element from which it was emitted.

The EDS X-ray detector measures the relative abundance of emitted X-rays versus their energy. The detector is typically lithium-drifted silicon, solid-state device. When an incident X-ray strikes the detector, it creates a charge pulse that is proportional to the energy of the X-ray. The charge pulse is converted to a voltage pulse (which remains proportional to the X-ray energy) by a charge-sensitive preamplifier. The signal is then sent to a multichannel analyzer where the pulses are sorted by voltage. The energy, as determined from the voltage measurement for each incident X-ray is sent to a computer for display and further data evaluation. The spectrum of X-ray energy versus counts is evaluated to determine the elemental composition of the sampled volume. Simple EDS system is shown in following fig 3.9. The compositional analysis of the nanocomposite thin films was performed using energy dispersive X-ray spectroscopy (EDXs).

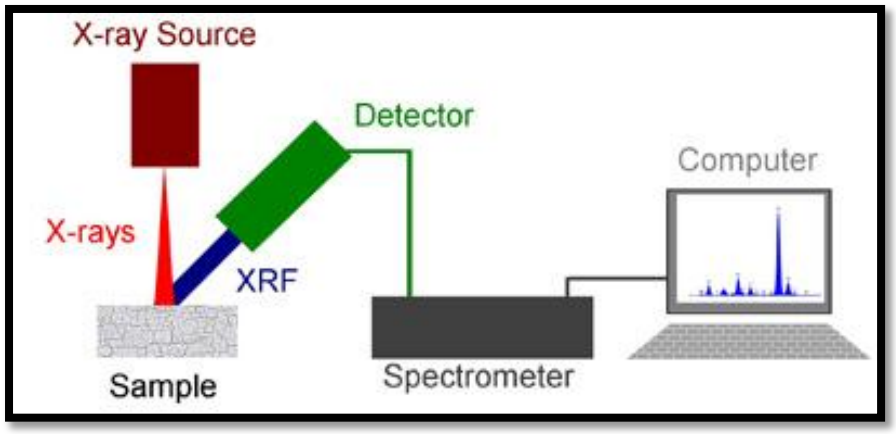

Figure 3.9 Schematic of EDS system

CHAPTER 4

RESULT AND DISCUSSION

4.1 PHASE CHARACTERIZATION

Figure 4.1(a) and fig 4.1 (b) shows the X-ray diffraction (XRD) pattern of BFO and BFO-CFO thin films annealed at 650ºC for 1 h. All the peaks in the pattern of pure BFO thin films show the perovskite-type structure with distorted rhombohedral symmetry (JCPDS card No. 20-0169, space group R3c). However it is clear from the fig 4.1(b) that the BFO-CFO XRD pattern can be separated into two evident set of well-defined peaks, one of which belongs to the perovskite antiferromagnetic structure and other to the cubic spinal ferrimagnetic CFO phase. The average grain size calculated by Scherrer formula was found to be 90 nm and 60 nm for BFO and CFO respectively. No other impurity phases such as $Bi_{25}FeO_{40}$ and $Bi_{46}Fe_2O_{70}$ were observed in pure BFO and BFO-CFO composite thin films structure.

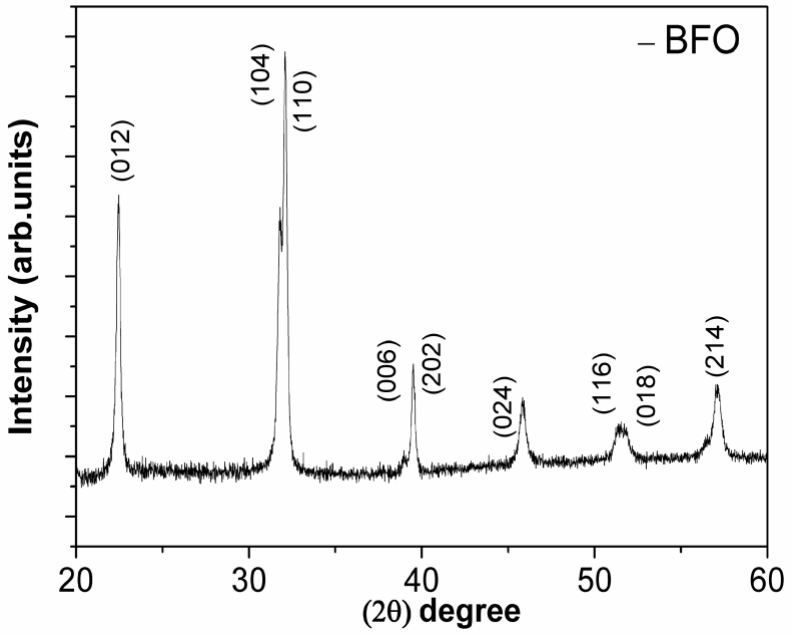

Figure 4.1 (a) XRD pattern for pure BFO thin film.

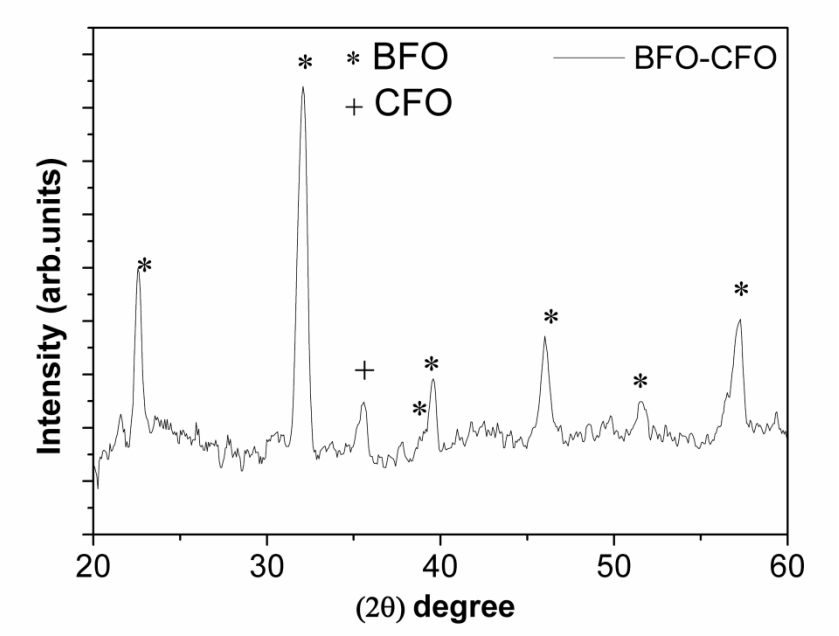

Figure 4.1 (b) XRD patterns for BFO-CFO composite thin film.

4.2 AFM ANALYSIS

Figure 4.2 (a-c) and fig 4.3 (a-c) shows the AFM images of pure BFO BFO/CFO composite thin films respectively at different magnifications. It clearly shows that BFO film shows smooth and uniform surface however BFO/CFO (0.9/0.1) films consist of randomly distributed fine CFO particles in BFO matrix. RMS Roughness of films was calculated as 2.9 nm and 3.8 nm for pure BFO and BFO-CFO thin films respectively.

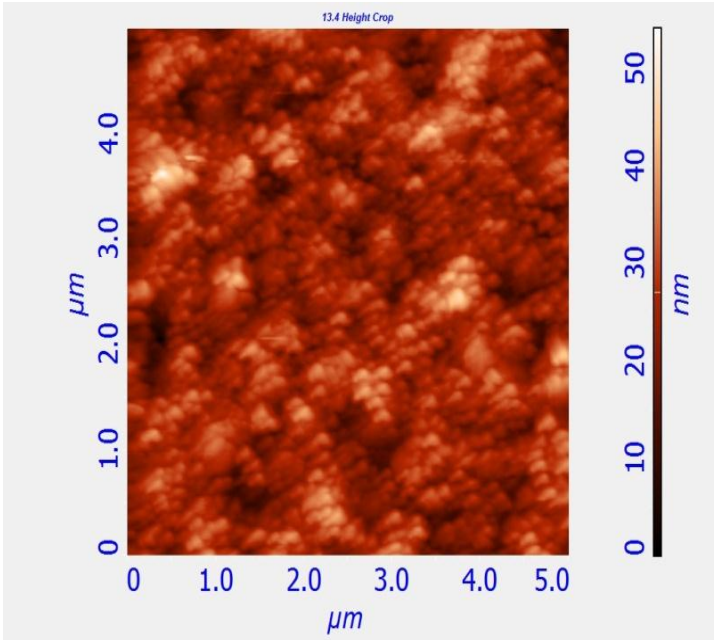

Figure 4.2 (a)

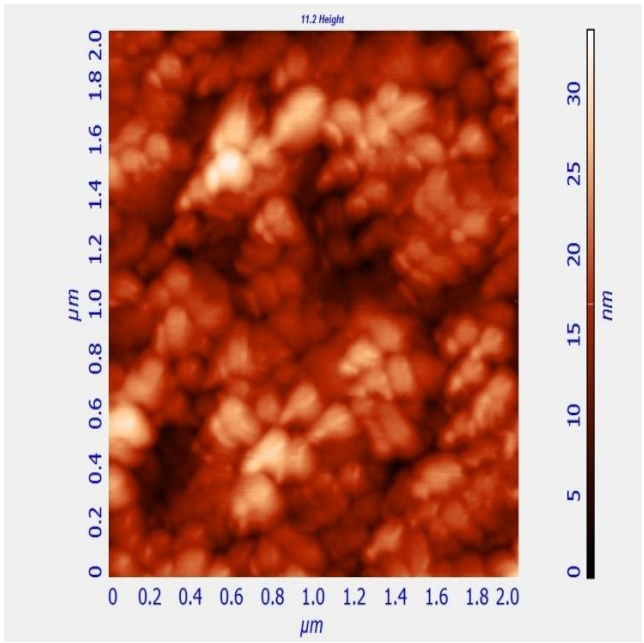

Figure 4.2 (b)

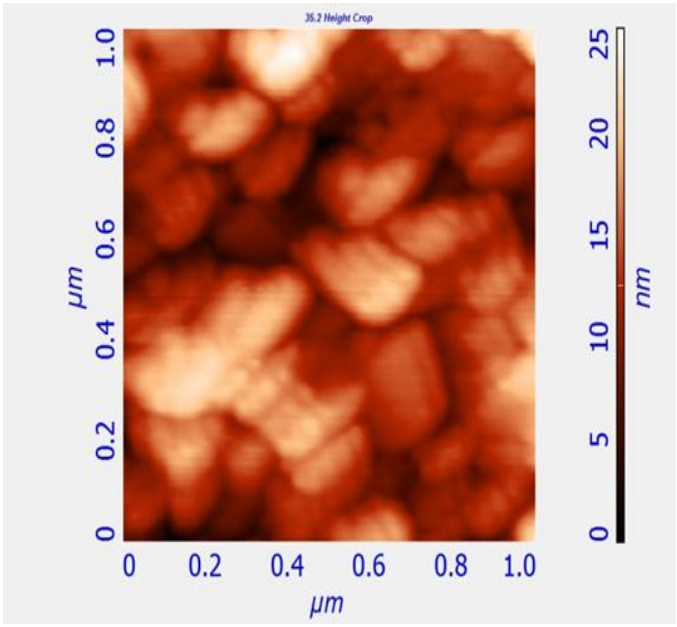

Figure 4.2 (c)

Figure 4.2 AFM images of pure BFO thin film at different magnification.

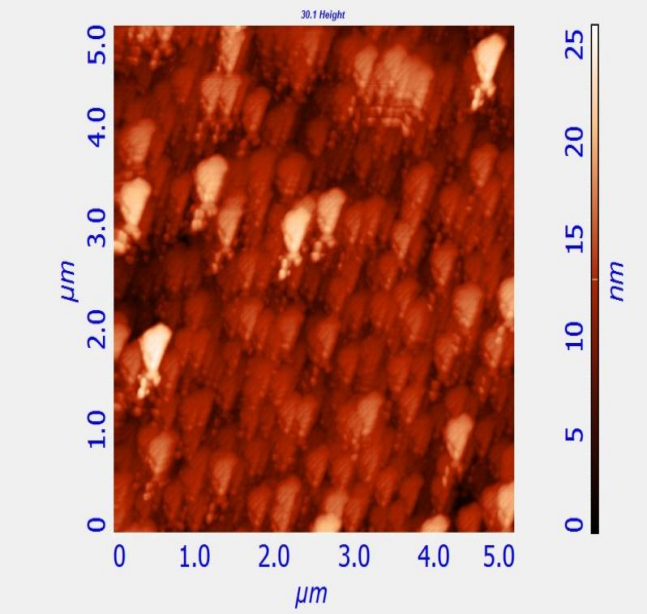

Figure 4.3 (a)

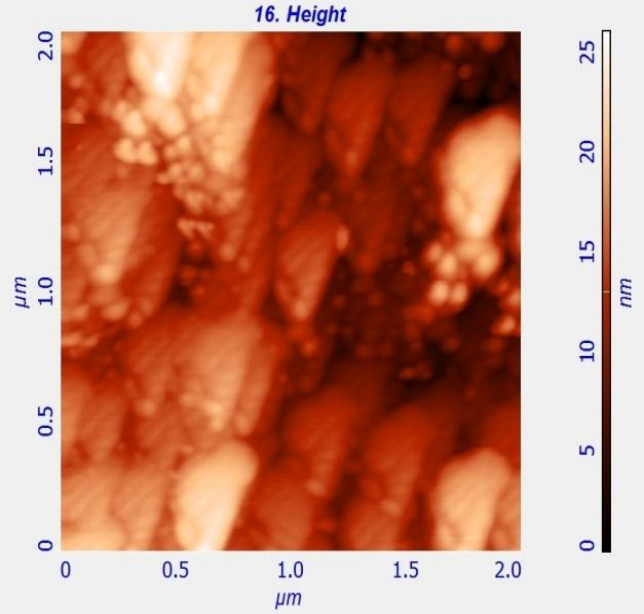

Figure 4.3 (b)

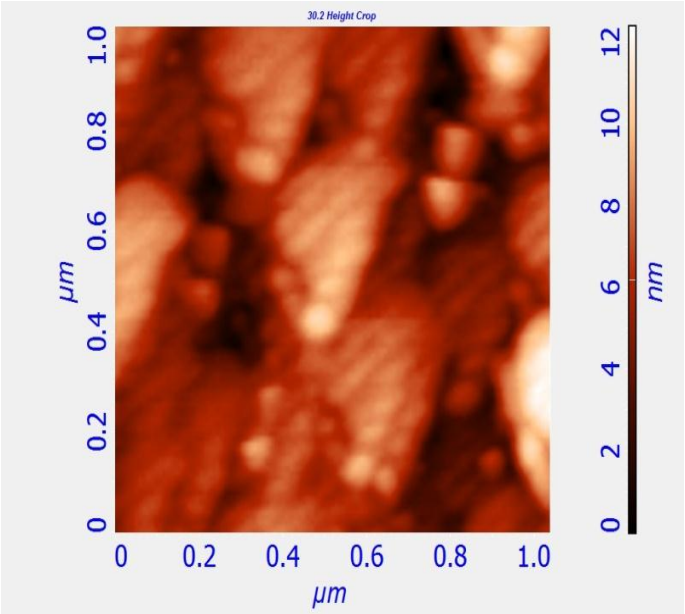

Figure 4.3 (c)

Figure 4.3 AFM images of BFO/CFO composite thin films at different magnification.

4.3 ENERGY DISPERSIVE X-RAY SPECTROSCOPY (EDS)

The Energy dispersive X-ray spectroscopy (EDXS) of BFO/CFO (0.9/0.1) composite thin films is shown in fig 4.4 and EDX spectrum confirmed the presence of all Bi, Co, and Fe elements at nearly expected elemental composition.

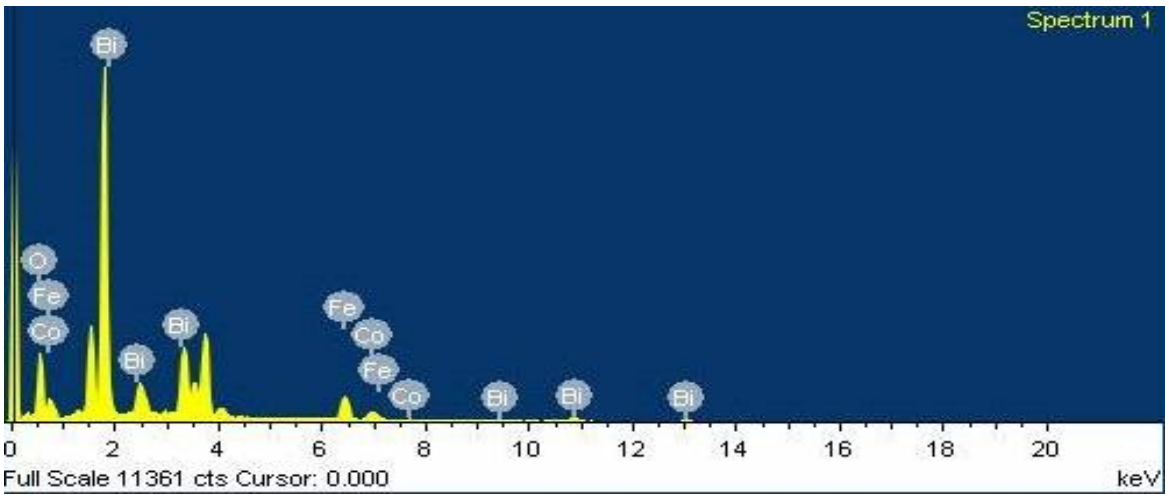

Figure 4.4 Energy Dispersive Spectroscopy of BFO/CFO composite thin filM.

4.4 P-E LOOP MEASUREMENT

Figure 4.5 shows the polarization vs. applied electric field (P - E) hysteresis loops of the pure BFO and the BFO/CFO composite thin films measured at room temperature as a function of volume ratio of CFO at 1Hz. The BFO and BFO/CFO (0.9/0.1) composite thin films show the desirable ferroelectric behavior. The P_r value measured for the pure BFO and BFO/CFO (0.9/0.1) thin films are 15μC/cm^2 and 10μC/cm^2 respectively.

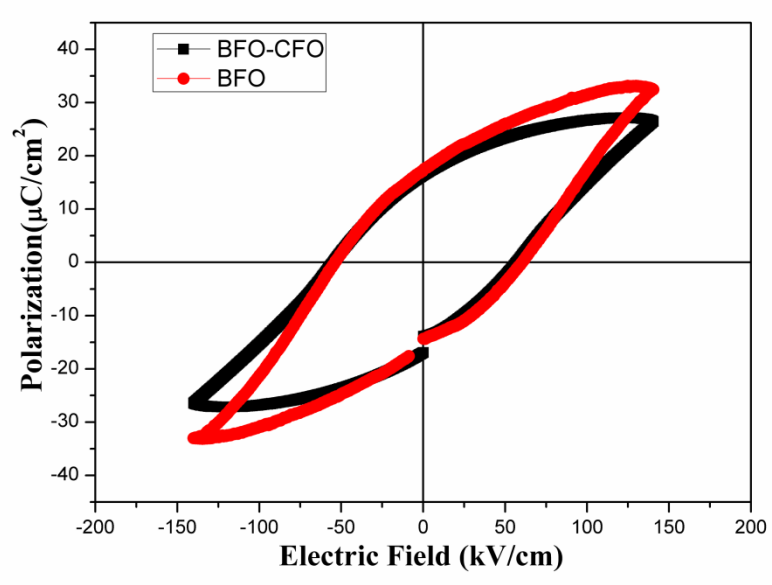

Figure 4.5 P-E Loop for pure BFO and composite BFO-CFO thin film.

4.5 MAGNETIC MEASUREMENT (SQUID)

Figure 4.6 shows the in plane magnetic behavior of all the samples with varying volume concentration of CFO at 300K. Pure BFO thin film clearly shows the antiferromagnetic behavior. Whereas, the well-defined magnetic hysteresis loop, indicating the presence of FM/AFM exchange coupling in the mixed perovskite-spinel system was observed in BFO/CFO composite thin films. The volume ratio of CFO nanoparticle in the BFO/CFO composite thin films strongly affects the magnetic properties of BFO/CFO. The M_s and H_c values of BFO/CFO composite thin films are much larger than that of pure BFO thin films and increases with increase in the volume ratio of cobalt ferrite together via exchange coupling between BFO and CFO. The values of M_s and H_c were found to be M_s = 40.12 emu/cm^3 and H_c= 127 Oe respectively.

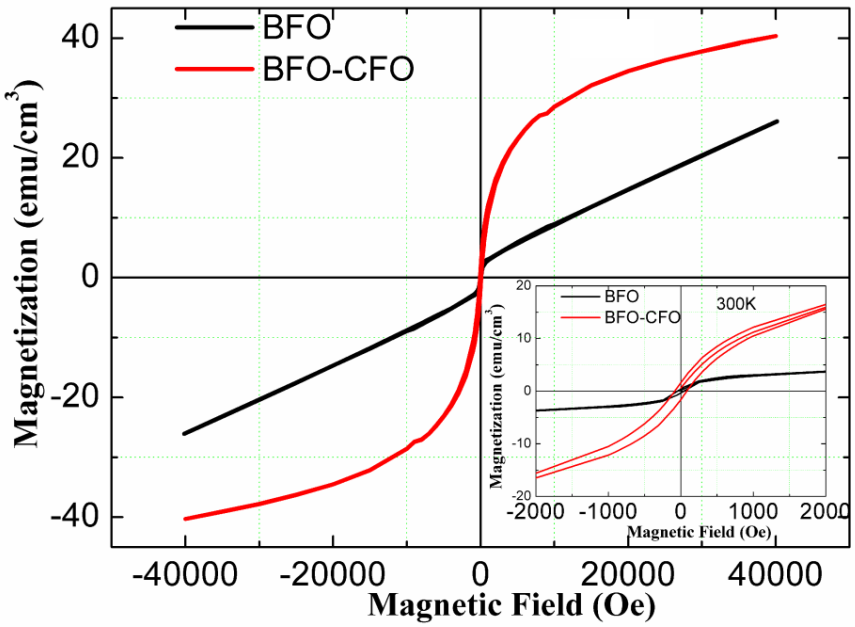

Figure 4.6 Magnetic hysteresis loops of pure BFO and BFO/CFO composite thin films at 300K.

CONCLUSION

In summary, multiferroic (1-x) $BiFeO_3$ – x $CoFe_2O_4$ (x = 0, 0.1) composite thin films were successfully synthesized by spin coating method in which two antiferromagnetic and ferromagnetic phases were deposited on Pt/SiO_2 substrate. XRD and EDXs examinations confirm the co-existence of both phases. The AFM images also indicate that the CFO grains are uniformly distributed in the BFO matrix. The magnetic properties of BFO/CFO composite thin films are strongly dependent on CFO, and exhibit an enhancement in the magnetic properties than pure BFO. The composite (1-x) $BiFeO_3$-x $CoFe_2O_4$ (x = 0.1) exhibited the M_s ~ 40.12 emu/cm^3 and H_c = 127 Oe at 300K. The P-E loop measurement showed a saturated hysteresis loop in both BFO and BFO-CFO composite thin films. However, ferroelectricity is found to be decreased in BFO-CFO composite thin films. The paraelectric CFO is responsible for decreasing ferroelectric behaviour.

REFERENCES

1. P.Curie, J. Phys. **3**, 393 (1894).

2. M. Fiebig, J. Phys. D: Appl. Phys. **38**, 8 (2005).

3. W. Eerenstein, N. D. Mathur and J. F. Scott, Nature Materials **442**, 759 (2006).

4. J. P. Rivera, Ferroelectrics **161**, 165 (1994).

5. R.Y. Zheng, X.S. Gao, Z.H. Zhou, and J. Wang, J. Appl. Phys. **101**, 054104-1 (2007).

6. J. Wang, J.B. Neaton, H. Zheng, V. Nagarajan, S. B. Ogale, B. Liu, D. Viehland, V. Vaithyanathan, D.G. Schlom, U.V. Waghmare, N.A. Spaldin, K.M. Rabe, M. Wuttig, and R. Ramesh, Science (www.sciencemag.org) **299**, 1719 (2003).

7. S. Y. Yang, F. Zavaliche, L. Mohaddes-Ardabili, V. Vaithyanathan, D.G. Schlom, Y.J. Lee, Y.H. Chu, M.P. Cruz, Q. Zhan, T. Zhao, and R. Ramesh, Appl. Phys. Lett. **87**, 102903-1 (2005).

8. H. Naganuma, Y. Inoue and S. Okamura, IEEE Trans. **55**, 1046 (2008).

9. N. C. Pramanik, T. Fujii, M. Nakanishi, "J. Takada, J. Math. Chem.**14**, 3328 (2004).

10. L. Yan, Z. Xing, Z. Wang, T. Wang, G. Lei, J. Li, D. Viehland, Appl. Phys. Lett. **94**, 192902-1 (2009).

11. Y. S. Oh, S. Crane, H. Zheng, Y. H. Chu, R. Ramesh, and K. H. Kim, Appl. Phys. Lett. **97**, 052902-1(2010).

12. T. Kimura et al., Nature **426**, 55 (2003).

13. N. Hur, S. Park, P. A. Sharma, J. S. Ahn, S. Guha, S.W. Cheong, Nature **429**, 392(2004).

14. 'Introduction to Solid State Physics' C.A. Kittel in seventh edition of John Wiley & Sons, Inc., New York publication (1996).

15. C. Michel, J. M. Moreau, G. D. Achenbach, R. Gerson and W. J. James, Solid State Comm. **7**, 701 (1969).

16. C. Ederer and N. A. Spaldin, Phys. Rev. B **71**, 060401 (2005).

17. D. Lebeugle, D. Colson, A. Forget and M. Viret, Appl. Phys. Lett. **91**, 022907 (2007).

18. I. Dzyaloshinskii, J. Phys. Chem. Solids **4**, 241 (1958).

19. T. Moriya, Phys. Rev. **120**, 91 (1960).

20. F. Zavaliche, P. Shafer and R. Ramesh, Applied phy. Lett. **87**, 252902 (2005).

21. E. J. Speranskaya, V. M. Skorikov, E. Ya. Kode, V. A. Terektova, Bull. Acad. Sci. **5**, 873 (1965).

22. M. I. Morozov, N. A. Lomanova, V. V. Gusarov, Russ. J. Gen. Chem. **73**, 1680 (2003).

23. R. Palai, R. S. Katiyar, H. Schmid, P. Tissot, S. J. Clark, J. Robertson, S. A. T. Redfern, G. Catalan, J. F. Scott, Phys. Rev. B **77**, 014110 (2008).

24. M. Valant, A. K. Axelsson, N. Alford, Chem. Mater. **19**, 5431 (2007).

25. N. N. Krainik, N. P. Khuchua, V. V. Zhdanova, V. A. Evseev, Sov, Phys. Solid State **8**, 654 (1966).

26. D. Lebeugle, Ph.D. Thesis Saclay Institute of Matter and Radiation (2007).

27. H. Bea, M. Bibes, A. Barthe´le´my, K. Bouzehouane, E. Jacquet, A. Khodan, J. P. Contour, Appl. Phys. Lett. **87**, 072508 (2005).

28. 'Magnetostriction: Theory and Applications of Magnetoelasticity' E. du Trémolet de Lacheisserie in first edition of CRC Press, Boca Raton, FL, (1993).

29. K. B. Hathaway and A. E. Clark, MRS Bull. **18**, 34 (1993).

30. 'Pulsed Laser Deposition of Thin Films' D. B. Chrisey and G. K. Hubler of John Wiley & Sons, Inc., New York publication (1994).

31. 'Pulsed Laser Deposition of thin films: applications-lead growth of functional materials' R. Eason of John Wiley & Sons, Inc., New York publication (2007).

32. X.-M. Liu, S.-Y. Fua, C.-J. Huanga, Mater. Sci. and Engg. B **121**, 255 (2005).

33. J.-P. Zhou, H.-C. He, Z. Shi, G. Liu, C.-W. Nan, J. Appl. Phys. **100**, 094106 (2006).
34. S. W. Lee, Chul Sung Kim, J. Magn. Magn. Mater. **304**, e772 (2006).

35. X. L. Zhong, J. B. Wang, M. Liao, G. J. Huang, S. H. Xie, and Y. C. Zhoub, Appl. Phys. Lett. **90**, 152903 (2007).

36. A. Roy, M. Liu, X. Li, J. Lou, S. Zheng, K. Du, N. X. Sun, J. Appl. Phys. **102**, 083911 (2007).

37. H. Naganuma, N. Shimura, J. Miura, H. Shima, S. Yasui, J. Appl. Phys. **103**, 07E314 (2008).

38. R. Y. Zheng, J. Wang, S. Ramakrishna, J. Appl. Phys. **104**, 034106 (2008).

39. R. Muralidharan, N. Dix, V. Skumryev, M. Varela, F. Sánchez, and J. Fontcuberta, J. Appl. Phys. **103**, 07E301 (2008).

40. J. Wu, J. Wangb, J. Appl. Phys. **105**, 124107 (2009).

41. L. Yan, Z. Xing, Z. Wang, T. Wang, G. Lei, J. Li, D. Viehland, Appl. Phys. Lett. **94**, 192902 (2009).

42. Y. Zhu, J. Cheng, S. Yu, W. Wu and Z. Meng, Appl. Phys. Lett. **96**, 19223 (2010).

43. W. Chen, W. Zhu, X. f. Chen, Z. Wang, J. Am. Ceram. Soc. **93**, 796 (2010).

44. I. Stern, J. He, X. Zhou, P. Silwal, L. Miao, J. M. Vargas, L. Spinu, D. H. Kim, Appl. Phys. Lett. **99**, 082908 (2011).

45. N. M. Aimon, Dong Hun Kim, Hong Kyoon Choi, C. A. Ross, Appl. Phys. Lett. **100**, 092901 (2012).

46. Keita Sone, Sho Sekiguchi, Hiroshi Naganuma, Takamichi Miyazaki, J. Appl. Phys. **111**, 124101 (2012).

47. Y. Li, Y. Yang, J. Yao, R. Viswan, Z. Wang, J. Li and D. Viehland, Appl. Phys. Lett. **101**, 022905 (2012).

48. 'Elements of X-ray Diffraction' B. D. Cullity and S. R. Stock in second edition of Addison-Wesley publication (1978).

49. G. Binning, C. F. Quate, Ch. Gerber. Phys. Rev. Lett. **56 (9)**, 930 (1986).